NANO LETTERS

pubs.acs.org/NanoLett Letter

Bound State in the Continuum in Nanoantenna-Coupled Slab Waveguide Enables Low-Threshold Quantum-Dot Lasing

Mengfei Wu, Lu Ding, Randy P. Sabatini, Laxmi Kishore Sagar, Golam Bappi, Ramón Paniagua-Domínguez, Edward H. Sargent,* and Arseniy I. Kuznetsov*

Cite This: https://doi.org/10.1021/acs.nanolett.1c03696 Read Online

ACCESS | Metrics & More | Article Recommendations | Supporting Information

ABSTRACT: Colloidal quantum dots (CQDs) are a promising gain material for solution-processed, wavelength-tunable lasers, with potential application in displays, communications, and biomedical devices. In this work, we combine a CQD film with an array of nanoantennas, made of titanium dioxide cylinders, to achieve lasing via bound states in the continuum (BICs). Here, the BICs are symmetry-protected cavity modes with giant quality factors, arising from slab waveguide modes in the planar CQD film, coupled to the periodic nanoantenna array. We engineer the thickness of the CQD film and size of the nanoantennas to achieve a BIC with good spatial and spectral overlap with the CQDs, based on a second-order transverse-electric (TE)-polarized waveguide mode. We obtain room-temperature lasing with a low threshold of approximately 11 kW/cm^2 (peak intensity) under 5-ns-pulsed optical excitation. This work sheds light on the optical modes in solution-processed, distributed-feedback lasers and highlights BICs as effective, versatile, surface-emitting lasing modes.

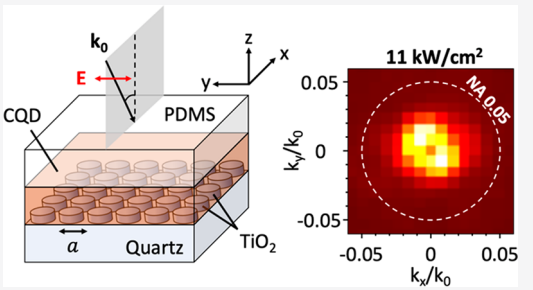

KEYWORDS: *colloidal quantum dots, lasing, bound state in the continuum, slab waveguide, distributed-feedback cavity, dielectric nanoantennas*

Solution-processed lasers, such as those made using colloidal quantum dots (CQDs),[1−7] colloidal quantum wells,[8−11] and perovskites,[12−14] possess wide spectral tunability and a compact, flexible form factor and are of interest for display, communications, sensing, and biomedical applications. Significant material innovations have led to continuous-wave (CW), solution-processed lasers at or close to room temperature, with a threshold pump intensity ranging from ∼100 W/cm^2 to ∼10 kW/cm^2.[3,8,13] Breakthroughs derived from innovations in optical design have also been reported.[10,15]

In general, a low-threshold laser requires not only an optical cavity with minimal absorption or radiation loss, and hence a high quality (Q) factor, but also good spatial and spectral overlap between the cavity mode and gain material to ensure efficient light−matter interaction. In previous solution-processed lasers, distributed-feedback (DFB)[2−4,12,13] and Fabry−Pérot[1,8,9] cavities have been employed extensively. A Fabry−Pérot cavity can possess a high Q factor and can position the gain material at the field maximum; however, fabrication of a high-Q device is challenging because of the large number of layers required and the need for precisely controlled layer thicknesses. A DFB cavity, on the other hand, typically consists of a grating made of a dielectric, coated with a solid film of gain material. The spatial mode-gain overlap extends laterally across the entire device, and the in-plane reflections (as a result of the periodic variation in the refractive index) can produce a high Q factor when the number of periods is large. Commercially available DFB lasers made of III−V semiconductors rely on the fundamental DFB mode, which involves a phase shift of π per period, to achieve edge lasing. In contrast, reported solution-processed lasers have largely relied on the second-order DFB mode, which contains a phase shift of 2π per period. While optical feedback is in plane, a second-order DFB can couple light out of plane via diffraction to achieve lasing in the normal direction.

Upon closer examination, the second-order DFB involves two distinct band-edge modes with different field distributions, representing the two ways a standing wave could be formed from two counter-propagating waves in the grating. This is illustrated for transverse-electric (TE)-polarized modes in Figures 1a and 1b, which plot the y-component of the electric field of the standing wave along a grating. The field of the mode in Figure 1a has the same symmetry as that of a plane wave at normal incidence (e.g., with respect to a y−z plane cutting in the middle of a unit cell); the mode can thus couple to the far field by diffraction. In contrast, the mode in Figure 1b has a different symmetry than the plane wave and therefore

Received: September 24, 2021
Revised: November 9, 2021

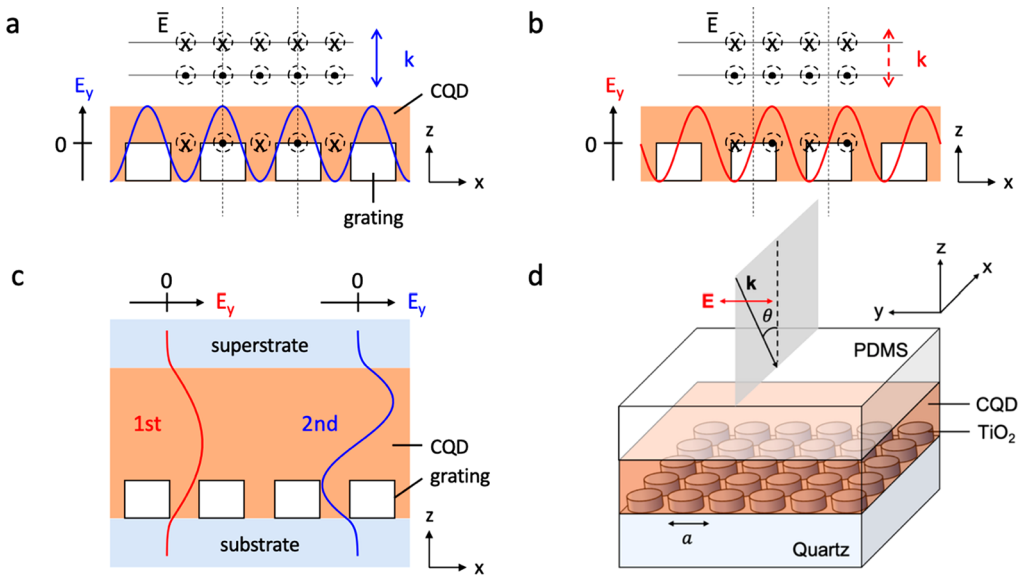

Figure 1. (a, b) Schematic showing two distinct second-order DFB modes with transverse-electric (TE) polarization: (a) diffraction-coupled band-edge mode; (b) bound state in the continuum (BIC). The *y*-component of the electric field (E_y) is plotted for the standing wave along the *x* direction of the grating. The direction of the electric field ($\bar{E}$) is indicated for the standing wave as well as the plane wave incident on the structure in the normal direction. The field of a BIC has a different symmetry compared to that of the plane wave, so a BIC is decoupled from the far field and has zero radiation loss. The solid and dashed arrows for the k vector in parts a and b denote allowed and forbidden radiation in the normal direction, respectively. CQD: colloidal quantum dot. (c) Sketch of E_y along the transverse (*z*) direction for the first- and second-order slab waveguide modes supported in the grating coated with a relatively thick layer of CQDs. (d) Device structure of the CQD laser in this work. The TiO_2 cylinders are 120 nm in height, and the period of the square array, *a*, is tuned with the cylinder diameter, keeping the gap between the cylinders fixed at 40 nm. The CQD film is about 300 nm in thickness. Optical measurements are taken in the *x*−*z* plane with TE polarization.

cannot couple to the far field in the normal direction. With a lower radiation loss, the mode in Figure 1b should have a higher Q factor. In fact, its Q factor could be infinite in theory for an ideal system without any absorption, scattering, or diffractive losses. Such a mode is known as a symmetry-protected bound state in the continuum (BIC).[16−20]

Taking advantage of the impressive Q factors, BICs have been utilized to achieve lasing in III−V semiconductors,[21−27] colloidal quantum wells,[11] perovskites,[14,28] and organics.[29,30] Early reports on CQD lasers,[2−6] however, did not differentiate between a BIC and a diffractively coupled band-edge mode. In the present work, we show that lasing occurs through symmetry-protected BICs, by experimentally determining the dispersion diagram (i.e., the photonic band structure). In addition, we engineer the CQD film thickness so that the grating-CQD slab supports not only first-order but also second-order waveguide modes (Figure 1c). We show that the BIC arising from a second-order waveguide mode gives a lower lasing threshold, thanks to better spatial mode-gain overlap. This leads to room-temperature lasing under 5-ns-pulsed optical excitation with a threshold peak intensity of approximately 11 kW/cm^2. The threshold is similar to those of reported BIC lasers pumped under comparable conditions[24,27] (see Table S1 in the Supporting Information for details).

In the CQD laser reported herein (Figure 1d), the grating is a 2D square array of titanium dioxide (TiO_2) cylinders,[31,32] with a height of 120 nm and a gap of 40 nm between cylinders in both the *x* and *y* directions; see Figure S1 in the Supporting Information for an SEM image of a representative array. Keeping the gap distance constant, we adjust the period of the grating by changing the diameter of the cylinders. Here, we use TiO_2 instead of the typical silicon dioxide (SiO_2) in earlier reports of DFB lasers since, with the relatively high refractive index of TiO_2 ($n \sim 2.5$), Mie resonances can be excited efficiently in the cylinders, transforming them into nano-antennas.[33−35] This enhances the optical intensity in the near field, thus allowing stronger light−matter interaction. The CQDs spin-coated on the TiO_2 grating have been engineered to facilitate population inversion and hence lower the optical gain threshold.[3] They consist of a cadmium selenide (CdSe) core and an asymmetric cadmium sulfide (CdS) shell capped with chloride ligands (see Methods in the Supporting Information for details). These CQDs can achieve amplified spontaneous emission (ASE) under stripe pump at low thresholds; Figure S2 in the Supporting Information shows a CQD film reaching ASE at ∼35 kW/cm^2. The refractive index of these CQDs is ∼1.9 at visible wavelengths, as measured using spectroscopic ellipsometry. Upon spin-coating, the CQD film is approximately 300 nm thick on a plain (grating-free) area, as measured using a profilometer. The sample is then capped with a layer of polydimethylsiloxane (PDMS, ∼1 mm thick), whose refractive index is similar to that of the quartz substrate ($n \sim 1.5$).

Given the thickness and refractive indices, the combined CQD-TiO_2 slab is able to support first- and second-order waveguide modes. For both modes, at a given frequency, the grating periodicity can be tuned so that the longitudinal (in-plane) component of the wave vector gives a phase delay of 2π per period of the grating. Under these conditions, counter-propagating waves form a standing wave, resulting in either a band-edge mode radiating in the normal direction via diffraction or a symmetry-protected BIC with no (or suppressed) radiation in the normal direction. The two modes have a slight energy difference owing to the different localizations of the field in the grating, giving rise to a band gap at the Γ point in the dispersion diagram.

https://doi.org/10.1021/acs.nanolett.1c03696
Nano Lett. XXXX, XXX, XXX−XXX

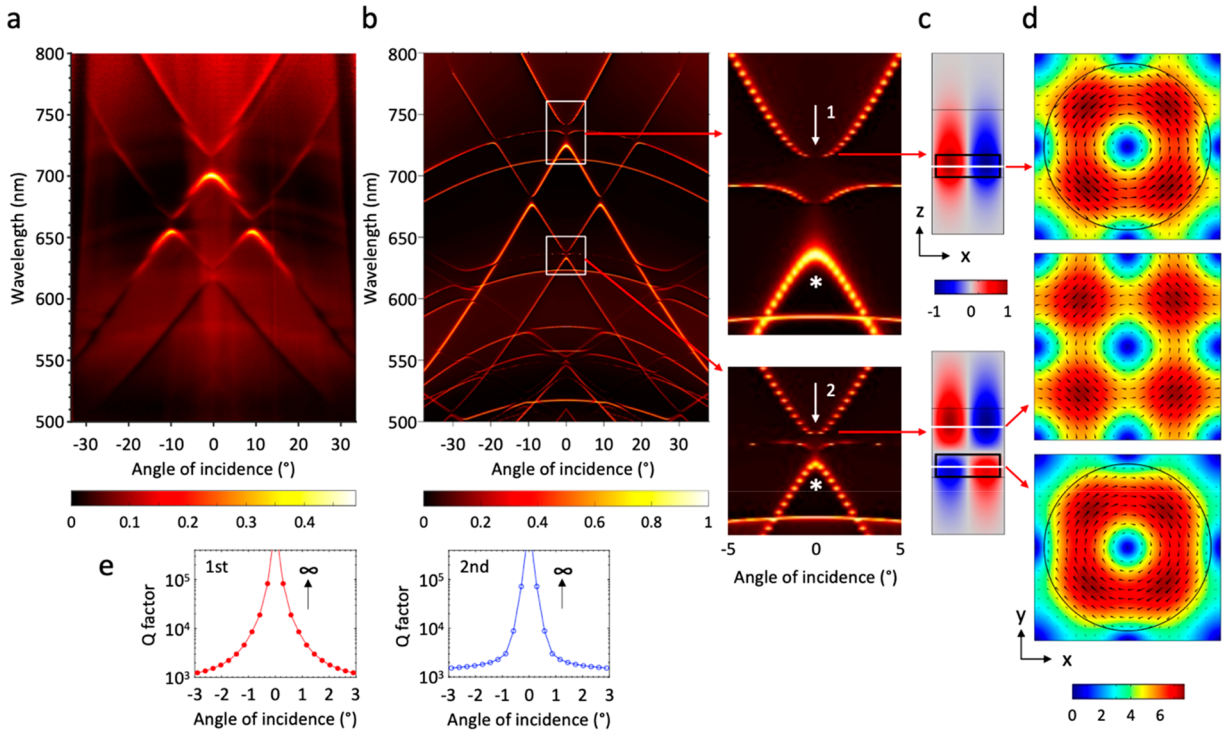

Figure 2. (a) Angle-resolved reflectance spectrum measured for a CQD-coated TiO_2 nanoantenna array with a cylinder diameter of 340 nm, under TE-polarized incident light. (b) Corresponding reflectance spectrum obtained by numerical simulations, assuming no absorption, flat surfaces, and infinite array size. The regions of interest are boxed and magnified for clarity, showing bands arising from the first- and second-order slab waveguide modes in the upper and lower panels, respectively. Arrows point to BICs, while asterisks (*) indicate diffraction-coupled band-edge modes. (c) The y-component of the electric field (E_y) plotted in the $x-z$ plane cut along the middle of a unit cell for the two BICs. (d) Amplitude (color map) and polarization vectors (arrows) of the electric field plotted in the $x-y$ plane cut along the white lines indicated in part c. The TiO_2 cylinders are outlined in black in parts c and d. (e) Quality (Q) factor as a function of the incident angle in the vicinity of the first- (left) and second-order (right) BICs, derived from part b. The Q factors in practice are lower due to absorption, sample imperfection, and a finite sample size.

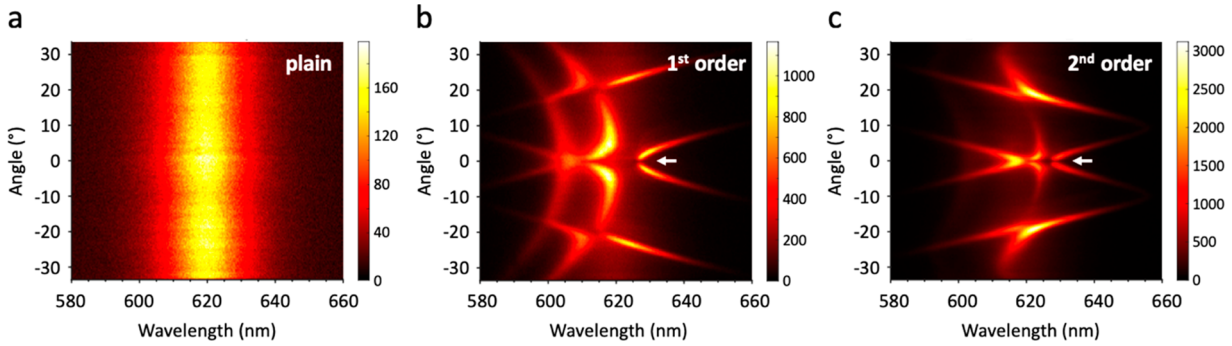

Figure 3. (a, b, c) Angle-resolved PL spectra of CQDs measured on (a) the plain area of the substrate and (b, c) a TiO_2 nanoantenna array with a cylinder diameter of (b) 280 nm and (c) 340 nm. The sample is excited with a continuous-wave laser at λ = 488 nm, and the PL is collected through a polarizer for TE-polarized light only. Parts b and c support BICs originating from the first- and second-order slab waveguide modes, respectively, marked by arrows.

To determine experimentally the photonic band structure of the sample, we measure the reflectance spectrum resolved in both wavelength and angle of incidence (or reflection), by projecting the back focal plane image through the slit of a spectrometer (see Methods in the Supporting Information for details). Figure 2a shows the reflectance spectrum of a CQD-coated TiO_2 nanoantenna array with a cylinder diameter of 340 nm and a period of 380 nm, when the incident light is TE-polarized. We observe bands arising from diffractive coupling of the first- and second-order waveguide modes, as well as vanishing reflectance at normal incidence near the band gaps, indicating the presence of BICs. To understand the optical modes better, we run a numerical simulation to obtain the more detailed dispersion diagram in Figure 2b. Here, we see salient features of several BICs at the Γ point (0°), where reflectance is inhibited since incident plane waves cannot couple to the BICs due to symmetry incompatibility.

The arrows in Figure 2b indicate the two BICs of interest, and eigenmode calculations give their mode profiles (Figures 2c and 2d for the side and top views of a unit cell, respectively). As expected, the BIC at $\lambda \sim 740$ nm arises from a first-order TE-polarized waveguide mode, while the BIC at $\lambda \sim 630$ nm originates from a second-order waveguide mode. The in-plane polarization vectors (Figure 2d) reveal a

https://doi.org/10.1021/acs.nanolett.1c03696
Nano Lett. XXXX, XXX, XXX−XXX

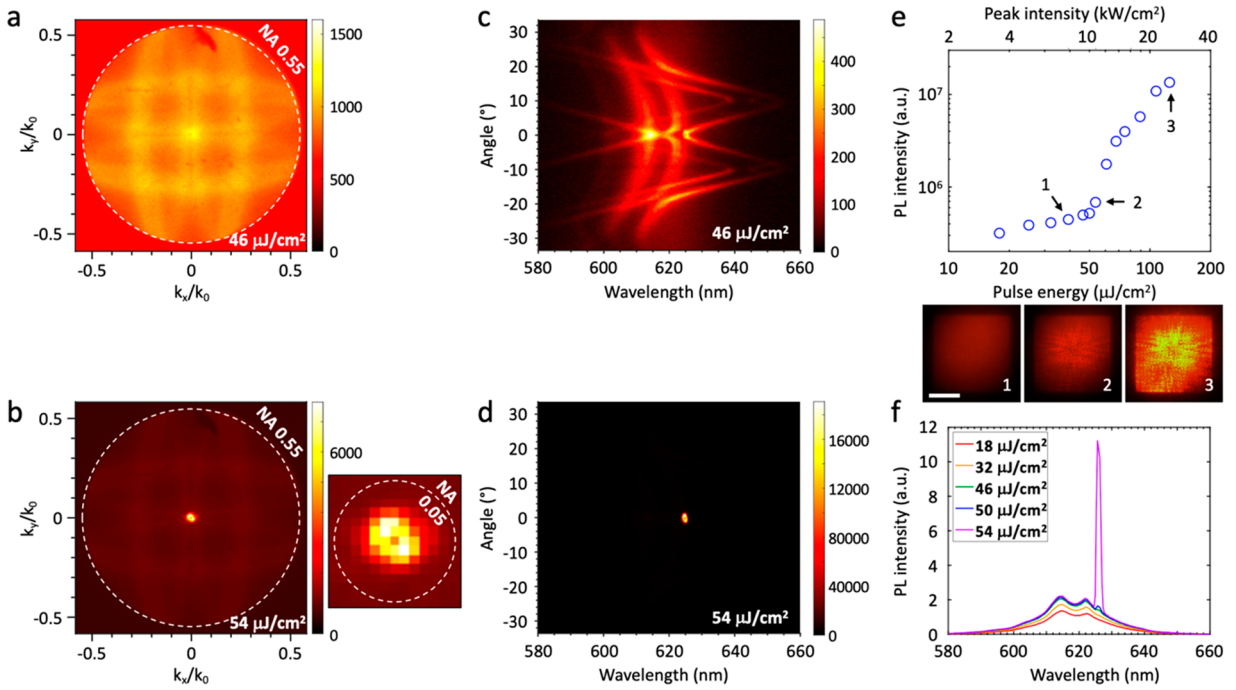

Figure 4. (a, b) Back focal plane image (radiation pattern) (a) below and (b) above the lasing threshold for a CQD-coated TiO_2 nanoantenna array with a cylinder diameter of 340 nm, at the pump fluence indicated. The structure supports a BIC arising from a second-order slab waveguide mode. The sample is excited by a pulsed laser (pulse width ~ 5 ns, repetition rate ~ 1250 Hz) at λ = 355 nm, and the PL is collected without a polarizer. The range of collection is limited by the numerical aperture (NA) of the objective. k_x/k_0 and k_y/k_0 are normalized in-plane wavevectors of the outcoupled light, indicating the direction of emission. The side panel in (b) is a zoomed-in image showing a donut-shaped radiation pattern in the normal direction. (c, d) Angle-resolved PL spectra (c) below and (d) above the lasing threshold at the pump fluence indicated, corresponding to (a) and (b) along k_x = 0, respectively. (e) Dependence of the CQD PL intensity on the pump fluence, plotted on a log−log scale, showing a lasing threshold of ~54 μJ/cm^2, equivalent to a peak intensity of ~11 kW/cm^2. The lower panel presents the fluorescence images of the array corresponding to the numbered data points. Scale bar: 20 μm. (f) PL spectra (integrated from −33° to 33°) at various pump fluences showing the onset of lasing.

circulating electric field, which is analogous to the field of an out-of-plane magnetic dipole. Thus, the BICs we observe here are similar to the previously reported BIC based on an array of magnetic dipoles oscillating in phase in the normal direction.[11,29,36]

Lastly, we derive the theoretical Q factors of the BICs from the dispersion diagram. Figure 2e shows that for each BIC, the Q factor increases toward infinity as the angle of incidence approaches zero. The simulation assumes that the extinction coefficients (κ) of all materials in the system are zero, all surfaces are smooth, and the periodic array is infinite in size. In reality, the CQDs have finite κ at visible wavelengths, the surface of the film is slightly undulating on top of the grating, and the array is 50 × 50 μm in size. As a result, the Q factors are finite for the BICs observed experimentally, also known as quasi-BICs.[16,17,37] Unfortunately, due to the limited resolution of our spectrometer (~2 nm; see Methods in the Supporting Information for details), we are unable to measure the high Q factors from the sample directly.

With the goal of achieving lasing, we first characterize the coupling of the CQD photoluminescence (PL) to the BICs under the excitation of a CW laser at λ = 488 nm. The angle-resolved PL spectrum of a plain CQD film (Figure 3a) shows an angle-independent PL centered at λ = 620 nm with a full width at half-maximum (fwhm) of 20 nm; see Figure S3 in the Supporting Information for a PL spectrum integrated across angles. We then seek to match the first- and second-order BICs spectrally to the CQD PL by varying the diameter of the TiO_2 cylinders, keeping the gap between cylinders fixed at 40 nm. The larger the cylinder diameter (i.e., the larger the grating period), the more red-shifted the optical modes, as the required in-plane propagation constant becomes lower for a given phase delay per period. For the cylinder array presented in Figure 2, the second-order BIC is in the desired spectral range (λ ~ 630 nm). To match the gain peak with the first-order BIC, however, the resonances must be blue-shifted. We find that when the cylinder diameter is reduced to 280 nm (period to 320 nm), the resonant wavelength of the first-order BIC is shifted to λ ~ 630 nm; see Figure S4 in the Supporting Information for a series of PL spectra for diameters ranging from 280 to 340 nm. Figures 3b and 3c contain the TE-polarized PL spectra of the CQD-coated arrays, with cylinder diameters of 280 and 340 nm, respectively, showing efficient coupling of the CQD PL to the various waveguide modes. In particular, we observe clear symmetry-protected BICs with a radiation node in the normal direction, namely the first- and second-order BICs in Figures 3b and 3c, respectively. The light emitted by the CQDs that is coupled to the BICs cannot radiate into the far field due to a mismatch in the field symmetry and is thus trapped in the cavity, providing efficient optical feedback for the CQDs. Furthermore, comparing Figures 3c and 2a, we notice that the PL map reflects the photonic bands more clearly than the reflectance map, potentially because of the additional enhancement in CQD emission by the Purcell effect.

To characterize lasing, we photoexcite the sample with a pulsed laser at λ = 355 nm (pulse width ~ 5 ns, repetition rate ~ 1250 Hz). We perform back focal plane (BFP) imaging to

https://doi.org/10.1021/acs.nanolett.1c03696
Nano Lett. XXXX, XXX, XXX−XXX

capture the PL intensity as a function of the emission angle, to a maximum angle of ∼33° limited by the numerical aperture of the collection objective (NA = 0.55). Figure 4a shows the BFP image of the unpolarized PL from the CQD-coated array with a cylinder diameter of 340 nm, supporting the second-order BIC. Here, we see the first- and second-order diffraction bands coupled to the CQD PL, with the first-order diffraction (i.e., second-order DFB) approaching the normal. As mentioned earlier, passing the BFP image through the slit of a spectrometer yields the angle- and wavelength-resolved PL spectrum. Figure 4c shows the PL analyzed spectrally along the y-axis of the BFP. At a pump fluence of 46 μJ/cm^2, we see some enhancement of the PL intensity at the second-order BIC, but the PL coupled to other bands is of a similar order of magnitude in intensity.

As we increase the pump fluence to 54 μJ/cm^2, the BFP image (Figure 4b) and the PL spectrum (Figure 4d) change dramatically. The PL intensity at the BIC increases by about 40 times, and lasing occurs at λ = 626 nm. Closer examination of the BFP image above the lasing threshold (Figure 4b, side panel) reveals a donut-shaped bright spot in the normal direction; see the angular distribution in Figure S5 in the Supporting Information. Intuitively, the donut shape is a result of suppressed radiation in the strict normal direction for the BIC but lasing radiation in the vicinity of the BIC, where a good balance exists between a high Q factor and an accessible radiation channel. Such a radiation pattern is characteristic of lasing through BICs based on dipoles oscillating normal to the lattice plane.[5,11,14,22,27,28] Indeed, as shown in Figure 2d, the waveguide-based BICs we observe here have electric fields similar to those of out-of-plane magnetic dipoles. Lastly, the light-in light-out curve (Figure 4e) and the PL spectra integrated across angles (Figure 4f) indicate a lasing threshold of ∼54 μJ/cm^2, corresponding to a peak intensity of about 11 kW/cm^2 for 5-ns pulses.

On the other hand, we also observe a lasing threshold of ∼150 μJ/cm^2 for the array with a cylinder diameter of 280 nm, via the first-order BIC; see Figure S6 in the Supporting Information for details. We note from Figure 2c that the field antinodes for the first-order BIC lie mainly inside the TiO_2 cylinder, while the field antinodes for the second-order BIC lie also in the CQD gain medium. As a result, the first-order BIC has poorer spatial overlap with the CQDs, which leads to a higher lasing threshold.

The threshold of 11 kW/cm^2, observed from the second-order BIC, is comparable to that of the CW lasing of the same type of CQDs reported earlier.[3] In the previous work, a 200 × 200 μm magnesium fluoride (MgF_2, $n \sim 1.4$) grating was used on a MgF_2 substrate cooled to about −20 °C.[3] Here, we use a smaller 50 × 50 μm TiO_2 nanoantenna array on a quartz substrate and at room temperature but photoexcited using 5-ns pulses at 1250 Hz instead of at CW. While it is unclear whether the previous CW study involved a diffractive band-edge mode or a BIC, in this work, we identify the lasing mode specifically as a BIC, based on a second-order slab waveguide mode. This type of mode possesses not only a giant Q factor but also good spatial overlap with the CQDs, allowing us to achieve low-threshold, room-temperature nanosecond lasing.

Although our study suggests that the high-Q BIC is more favorable for lasing than the diffraction-coupled band-edge mode, which is also observed in a previous study on plasmonic nanoparticle arrays,[38] it is important to note that more work is necessary to ascertain if BICs would indeed dominate (i.e., lead to a lower lasing threshold) under all circumstances, particularly given that the spatial mode-gain overlap can be better for the diffractive band-edge mode (Figure 1a) compared to the BIC (Figure 1b). Provided the spectral mode-gain overlap is similar, the competition between the Q factor and the spatial overlap would be interesting to explore. We advocate for characterization of lasing modes in detail, including the dispersion diagram and radiation pattern, for second-order DFB lasers in the future. Understanding the nature of the lasing cavity should be helpful not only for device optimization but also for applications. For instance, BIC lasers are promising as compact, on-chip sources of optical vortex beams,[14,39−41] with their far-field radiation carrying well-defined topological charges (i.e., polarization rotating about the beam axis; see Figure 2d). Vortex microlasers at optical frequencies offer potential benefits in optical communications and quantum information processing.

In conclusion, we report a low-threshold laser at room temperature, consisting of a ∼300-nm-thick film of CQDs covering a square array of TiO_2 cylindrical nanoantennas. Lasing is achieved from high-Q modes known as BICs, arising from first- and second-order TE-polarized slab waveguide modes, excited in the CQD-TiO_2 structure and coupled to the periodicity of the nanoantenna array. The second-order BIC, in particular, gives a low lasing threshold of approximately 11 kW/cm^2 under 5-ns-pulsed optical pumping, thanks to a high Q factor and good spatial mode-gain overlap. In addition, for what is conventionally termed a second-order DFB mode, we differentiate between a BIC and a band-edge mode coupled to diffraction. We show that BICs are the modes responsible for lasing in the (near) normal direction in our system and encourage researchers in the field to collectively verify if BICs, with their extraordinarily high Q factors, are the dominant lasing modes in second-order DFB lasers. Finally, we highlight the potential application of BIC lasers, with their exotic radiation patterns, as sources of optical vortex beams for communications and information processing.

■ ASSOCIATED CONTENT

Supporting Information

The Supporting Information is available free of charge at https://pubs.acs.org/doi/10.1021/acs.nanolett.1c03696.

Methods; table of comparison for BIC lasers; SEM image of a TiO_2 cylinder array; ASE threshold of a CQD film; integrated PL spectrum of a CQD film; angle-resolved PL spectra for a series of cylinder diameters; angular distribution of the lasing radiation from the second-order BIC; and lasing characterization of the first-order BIC (PDF)

■ AUTHOR INFORMATION

Corresponding Authors

Edward H. Sargent − *Department of Electrical and Computer Engineering, University of Toronto, Toronto, Ontario M5S 3G4, Canada;* orcid.org/0000-0003-0396-6495; Email: ted.sargent@utoronto.ca

Arseniy I. Kuznetsov − *Institute of Materials Research and Engineering, A*STAR (Agency for Science, Technology and Research), Singapore 138634, Singapore;* orcid.org/0000-0002-7622-8939; Email: arseniy_kuznetsov@imre.a-star.edu.sg

https://doi.org/10.1021/acs.nanolett.1c03696
Nano Lett. XXXX, XXX, XXX−XXX

Authors

Mengfei Wu − *Institute of Materials Research and Engineering, A*STAR (Agency for Science, Technology and Research), Singapore 138634, Singapore; Department of Electrical and Computer Engineering, University of Toronto, Toronto, Ontario M5S 3G4, Canada;* orcid.org/0000-0002-4728-3234

Lu Ding − *Institute of Materials Research and Engineering, A*STAR (Agency for Science, Technology and Research), Singapore 138634, Singapore;* orcid.org/0000-0001-8087-2738

Randy P. Sabatini − *Department of Electrical and Computer Engineering, University of Toronto, Toronto, Ontario M5S 3G4, Canada;* orcid.org/0000-0002-5975-4347

Laxmi Kishore Sagar − *Department of Electrical and Computer Engineering, University of Toronto, Toronto, Ontario M5S 3G4, Canada;* orcid.org/0000-0002-7656-7308

Golam Bappi − *Department of Electrical and Computer Engineering, University of Toronto, Toronto, Ontario M5S 3G4, Canada*

Ramón Paniagua-Domínguez − *Institute of Materials Research and Engineering, A*STAR (Agency for Science, Technology and Research), Singapore 138634, Singapore;* orcid.org/0000-0001-7836-681X

Complete contact information is available at: https://pubs.acs.org/10.1021/acs.nanolett.1c03696

Author Contributions

M.W. fabricated the sample, performed optical characterizations, and wrote the first draft of the manuscript. L.K.S. synthesized the colloidal quantum dots (CQDs). G.B. deposited the CQD film and helped with initial optical measurements. L.D. performed numerical simulations under the guidance of R.P.-D. R.P.S. provided technical guidance. E.H.S and A.I.K supervised the work. All authors contributed to writing the manuscript.

Notes

The authors declare no competing financial interest.

■ ACKNOWLEDGMENTS

This work was supported by the A*STAR SERC Pharos programme (grant number 152 73 00025; Singapore), AME Programmatic Grant No. A18A7b0058 (Singapore), National Research Foundation of Singapore under Grant No. NRF-NRFI2017-01, the Ontario Research Fund-Research Excellence Program, and the Natural Sciences and Engineering Research Council (NSERC) of Canada. In addition, M.W. acknowledges generous support from the Banting Postdoctoral Fellowship. The authors are grateful to Ha Son Tung and Joao Martins de Pina for assisting with optical characterizations, to Vytautas Valuckas for SEM characterization, and to Sjoerd Hoogland and Oleksandr Voznyy for helpful discussions.

■ REFERENCES

(1) Dang, C.; Lee, J.; Breen, C.; Steckel, J. S.; Coe-Sullivan, S.; Nurmikko, A. Red, Green and Blue Lasing Enabled by Single-Exciton Gain in Colloidal Quantum Dot Films. *Nat. Nanotechnol.* **2012**, *7*, 335−339.

(2) Adachi, M. M.; Fan, F.; Sellan, D. P.; Hoogland, S.; Voznyy, O.; Houtepen, A. J.; Parrish, K. D.; Kanjanaboos, P.; Malen, J. A.; Sargent, E. H. Microsecond-Sustained Lasing from Colloidal Quantum Dot Solids. *Nat. Commun.* **2015**, *6*, 8694.

(3) Fan, F.; Voznyy, O.; Sabatini, R. P.; Bicanic, K. T.; Adachi, M. M.; McBride, J. R.; Reid, K. R.; Park, Y. S.; Li, X.; Jain, A.; et al. Continuous-Wave Lasing in Colloidal Quantum Dot Solids Enabled by Facet-Selective Epitaxy. *Nature* **2017**, *544*, 75−79.

(4) Roh, J.; Park, Y. S.; Lim, J.; Klimov, V. I. Optically Pumped Colloidal-Quantum-Dot Lasing in LED-like Devices with an Integrated Optical Cavity. *Nat. Commun.* **2020**, *11*, 271.

(5) Guan, J.; Sagar, L. K.; Li, R.; Wang, D.; Bappi, G.; Wang, W.; Watkins, N.; Bourgeois, M. R.; Levina, L.; Fan, F.; et al. Quantum Dot-Plasmon Lasing with Controlled Polarization Patterns. *ACS Nano* **2020**, *14*, 3426−3433.

(6) Guan, J.; Sagar, L. K.; Li, R.; Wang, D.; Bappi, G.; Watkins, N. E.; Bourgeois, M. R.; Levina, L.; Fan, F.; Hoogland, S.; et al. Engineering Directionality in Quantum Dot Shell Lasing Using Plasmonic Lattices. *Nano Lett.* **2020**, *20*, 1468−1474.

(7) Park, Y. S.; Roh, J.; Diroll, B. T.; Schaller, R. D.; Klimov, V. I. Colloidal Quantum Dot Lasers. *Nat. Rev. Mater.* **2021**, *6*, 382−401.

(8) Grim, J. Q.; Christodoulou, S.; Di Stasio, F.; Krahne, R.; Cingolani, R.; Manna, L.; Moreels, I. Continuous-Wave Biexciton Lasing at Room Temperature Using Solution-Processed Quantum Wells. *Nat. Nanotechnol.* **2014**, *9*, 891−895.

(9) Guzelturk, B.; Kelestemur, Y.; Olutas, M.; Delikanli, S.; Demir, H. V. Amplified Spontaneous Emission and Lasing in Colloidal Nanoplatelets. *ACS Nano* **2014**, *8*, 6599−6605.

(10) Yang, Z.; Pelton, M.; Fedin, I.; Talapin, D. V.; Waks, E. A Room Temperature Continuous-Wave Nanolaser Using Colloidal Quantum Wells. *Nat. Commun.* **2017**, *8*, 143.

(11) Wu, M.; Ha, S. T.; Shendre, S.; Durmusoglu, E. G.; Koh, W. K.; Abujetas, D. R.; Sánchez-Gil, J. A.; Paniagua-Domínguez, R.; Demir, H. V.; Kuznetsov, A. I. Room-Temperature Lasing in Colloidal Nanoplatelets via Mie-Resonant Bound States in the Continuum. *Nano Lett.* **2020**, *20*, 6005−6011.

(12) Jia, Y.; Kerner, R. A.; Grede, A. J.; Rand, B. P.; Giebink, N. C. Continuous-Wave Lasing in an Organic-Inorganic Lead Halide Perovskite Semiconductor. *Nat. Photonics* **2017**, *11*, 784−788.

(13) Qin, C.; Sandanayaka, A. S. D.; Zhao, C.; Matsushima, T.; Zhang, D.; Fujihara, T.; Adachi, C. Stable Room-Temperature Continuous-Wave Lasing in Quasi-2D Perovskite Films. *Nature* **2020**, *585*, 53−57.

(14) Huang, C.; Zhang, C.; Xiao, S.; Wang, Y.; Fan, Y.; Liu, Y.; Zhang, N.; Qu, G.; Ji, H.; Han, J.; et al. Ultrafast Control of Vortex Microlasers. *Science* **2020**, *367*, 1018−1021.

(15) Fernandez-Bravo, A.; Wang, D.; Barnard, E. S.; Teitelboim, A.; Tajon, C.; Guan, J.; Schatz, G. C.; Cohen, B. E.; Chan, E. M.; Schuck, P. J.; et al. Ultralow-Threshold, Continuous-Wave Upconverting Lasing from Subwavelength Plasmons. *Nat. Mater.* **2019**, *18*, 1172−1176.

(16) Hsu, C. W.; Zhen, B.; Stone, A. D.; Joannopoulos, J. D.; Soljačić, M. Bound States in the Continuum. *Nat. Rev. Mater.* **2016**, *1*, 16048.

(17) Koshelev, K.; Favraud, G.; Bogdanov, A.; Kivshar, Y.; Fratalocchi, A. Nonradiating Photonics with Resonant Dielectric Nanostructures. *Nanophotonics* **2019**, *8*, 725−745.

(18) Sadrieva, Z.; Frizyuk, K.; Petrov, M.; Kivshar, Y.; Bogdanov, A. Multipolar Origin of Bound States in the Continuum. *Phys. Rev. B: Condens. Matter Mater. Phys.* **2019**, *100*, 115303.

(19) Azzam, S. I.; Shalaev, V. M.; Boltasseva, A.; Kildishev, A. V. Formation of Bound States in the Continuum in Hybrid Plasmonic-Photonic Systems. *Phys. Rev. Lett.* **2018**, *121*, 253901.

(20) Azzam, S. I.; Kildishev, A. V. Photonic Bound States in the Continuum: From Basics to Applications. *Adv. Opt. Mater.* **2021**, *9*, 2001469.

(21) Miyai, E.; Sakai, K.; Okano, T.; Kunishi, W.; Ohnishi, D.; Noda, S. Lasers Producing Tailored Beams. *Nature* **2006**, *441*, 946.

(22) Van Beijnum, F.; Van Veldhoven, P. J.; Geluk, E. J.; De Dood, M. J. A.; 't Hooft, G. W.; Van Exter, M. P. Surface Plasmon Lasing Observed in Metal Hole Arrays. *Phys. Rev. Lett.* **2013**, *110*, 206802.

(23) Hirose, K.; Liang, Y.; Kurosaka, Y.; Watanabe, A.; Sugiyama, T.; Noda, S. Watt-Class High-Power, High-Beam-Quality Photonic-Crystal Lasers. *Nat. Photonics* **2014**, *8*, 406−411.
(24) Kodigala, A.; Lepetit, T.; Gu, Q.; Bahari, B.; Fainman, Y.; Kante, B. Lasing Action from Photonic Bound States in Continuum. *Nature* **2017**, *541*, 196−199.
(25) Ha, S. T.; Fu, Y. H.; Emani, N. K.; Pan, Z.; Bakker, R. M.; Paniagua-Domínguez, R.; Kuznetsov, A. I. Directional Lasing in Resonant Semiconductor Nanoantenna Arrays. *Nat. Nanotechnol.* **2018**, *13*, 1042−1047.
(26) Mylnikov, V.; Ha, S. T.; Pan, Z.; Valuckas, V.; Paniagua-Domínguez, R.; Demir, H. V.; Kuznetsov, A. I. Lasing Action in Single Subwavelength Particles Supporting Supercavity Modes. *ACS Nano* **2020**, *14*, 7338−7346.
(27) Hwang, M.; Lee, H.; Kim, K.; Jeong, K.; Kwon, S.; Koshelev, K.; Kivshar, Y.; Park, H. Ultralow-Threshold Laser Using Super-Bound States in the Continuum. *Nat. Commun.* **2021**, *12*, 4135.
(28) Tian, J.; Adamo, G.; Liu, H.; Wu, M.; Klein, M.; Deng, J.; Ang, N. S. S.; Paniagua-Domínguez, R.; Liu, H.; Kuznetsov, A. I.; et al. Phase-Change Perovskite Tunable Microlaser. *arXiv:2107.05239.arXiv.org e-Print archive*, 2021, https://arxiv.org/abs/2107.05239 (accessed 2021-07-15).
(29) Azzam, S. I.; Chaudhuri, K.; Lagutchev, A.; Jacob, Z.; Kim, Y. L.; Shalaev, V. M.; Boltasseva, A.; Kildishev, A. V. Single and Multi-Mode Directional Lasing from Arrays of Dielectric Nanoresonators. *Laser Photonics Rev.* **2021**, *15*, 2000411.
(30) Yang, J. H.; Huang, Z. T.; Maksimov, D. N.; Pankin, P. S.; Timofeev, I. V.; Hong, K. B.; Li, H.; Chen, J. W.; Hsu, C. Y.; Liu, Y. Y.; et al. Low-Threshold Bound State in the Continuum Lasers in Hybrid Lattice Resonance Metasurfaces. *Laser Photonics Rev.* **2021**, *15*, 2100118.
(31) Khorasaninejad, M.; Chen, W. T.; Devlin, R. C.; Oh, J.; Zhu, A. Y.; Capasso, F. Metalenses at Visible Wavelengths: Diffraction-Limited Focusing and Subwavelength Resolution Imaging. *Science* **2016**, *352*, 1190−1194.
(32) Khaidarov, E.; Hao, H.; Paniagua-Domínguez, R.; Yu, Y. F.; Fu, Y. H.; Valuckas, V.; Yap, S. L. K.; Toh, Y. T.; Ng, J. S. K.; Kuznetsov, A. I. Asymmetric Nanoantennas for Ultrahigh Angle Broadband Visible Light Bending. *Nano Lett.* **2017**, *17*, 6267−6272.
(33) Kuznetsov, A. I.; Miroshnichenko, A. E.; Brongersma, M. L.; Kivshar, Y. S.; Luk'yanchuk, B. Optically Resonant Dielectric Nanostructures. *Science* **2016**, *354*, No. aag2472.
(34) Kruk, S.; Kivshar, Y. Functional Meta-Optics and Nanophotonics Governed by Mie Resonances. *ACS Photonics* **2017**, *4*, 2638−2649.
(35) Staude, I.; Pertsch, T.; Kivshar, Y. S. All-Dielectric Resonant Meta-Optics Lightens Up. *ACS Photonics* **2019**, *6*, 802−814.
(36) Murai, S.; Abujetas, D. R.; Castellanos, G. W.; Sánchez-Gil, J. A.; Zhang, F.; Rivas, J. G. Bound States in the Continuum in the Visible Emerging from Out-of-Plane Magnetic Dipoles. *ACS Photonics* **2020**, *7*, 2204−2210.
(37) Sadrieva, Z. F.; Sinev, I. S.; Koshelev, K. L.; Samusev, A.; Iorsh, I. V.; Takayama, O.; Malureanu, R.; Bogdanov, A. A.; Lavrinenko, A. V. Transition from Optical Bound States in the Continuum to Leaky Resonances: Role of Substrate and Roughness. *ACS Photonics* **2017**, *4*, 723−727.
(38) Hakala, T. K.; Rekola, H. T.; Väkeväinen, A. I.; Martikainen, J. P.; Nečada, M.; Moilanen, A. J.; Törmä, P. Lasing in Dark and Bright Modes of a Finite-Sized Plasmonic Lattice. *Nat. Commun.* **2017**, *8*, 13687.
(39) Zhen, B.; Hsu, C. W.; Lu, L.; Stone, A. D.; Soljačić, M. Topological Nature of Optical Bound States in the Continuum. *Phys. Rev. Lett.* **2014**, *113*, 257401.
(40) Doeleman, H. M.; Monticone, F.; Den Hollander, W.; Alù, A.; Koenderink, A. F. Experimental Observation of a Polarization Vortex at an Optical Bound State in the Continuum. *Nat. Photonics* **2018**, *12*, 397−401.
(41) Wang, B.; Liu, W.; Zhao, M.; Wang, J.; Zhang, Y.; Chen, A.; Guan, F.; Liu, X.; Shi, L.; Zi, J. Generating Optical Vortex Beams by Momentum-Space Polarization Vortices Centred at Bound States in the Continuum. *Nat. Photonics* **2020**, *14*, 623−628.

https://doi.org/10.1021/acs.nanolett.1c03696
Nano Lett. XXXX, XXX, XXX−XXX